Supplement of Clim. Past, 15, 91–104, 2019
https://doi.org/10.5194/cp-15-91-2019-supplement

Climate of the Past
Open Access
EGU

Supplement of

The 405 kyr and 2.4 Myr eccentricity components in Cenozoic carbon isotope records

Ilja J. Kocken et al.

Correspondence to: Ilja J. Kocken (i.j.kocken@uu.nl)

1 Calcite compensation depth outliers

The large number of very low values in the CCD can be explained by the steady state alternating between two or more sediment boxes. This could also be the cause of the relatively stronger precession and obliquity peaks in the CCD's spectrum (Fig. 3 (c)), wherein the large high-frequency perturbations overshadow the long-term trend. The identical spectral outcome of a medium noise-only run (supplement fig. 4) further substantiates this assessment. These issues could be resolved by increasing the limitation: the finite number of sediment boxes in the model to generate a smoother CCD curve.

2 Calcite compensation depth spectral analysis

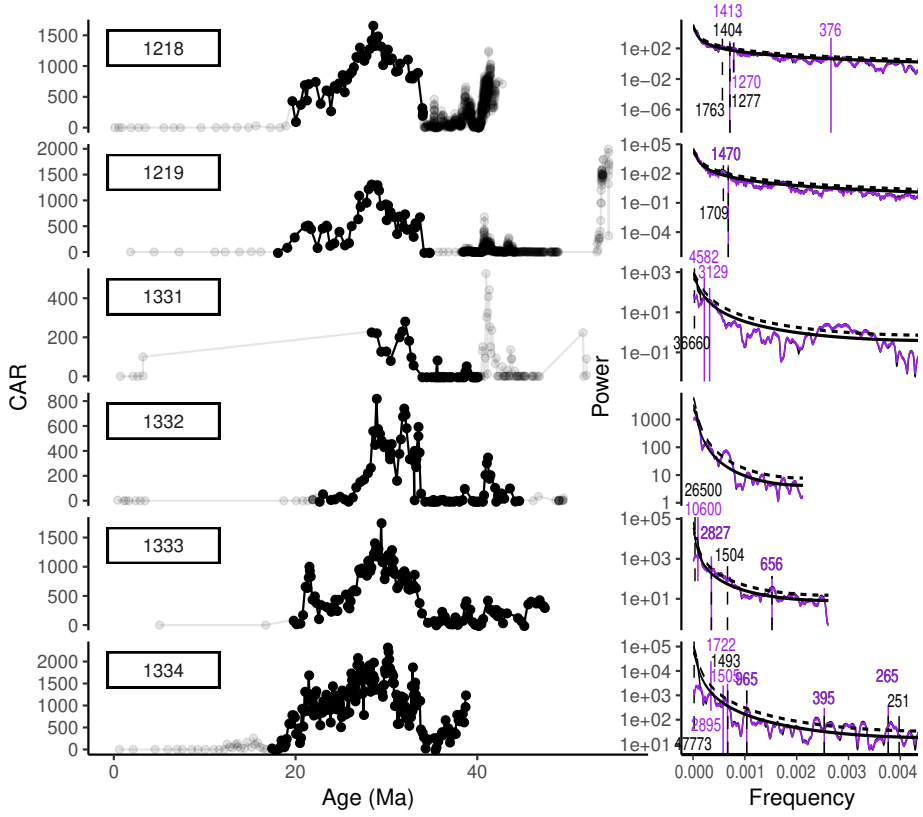

Figure 1. Carbonate accumulation rate (CAR) in the time (left side) and frequency domains (right side) for all sites in Pälike et al. (2012). Loess filtered (purple) and unfiltered (black) MTM-spectra are shown (right side) for the selected time-slices (darker dots in left side). Time-slices were selected based on continuous similar-resolution intervals where there are no known time-scale issues. Corresponding significant (harmonic f-test) peaks are labelled with associated periods.

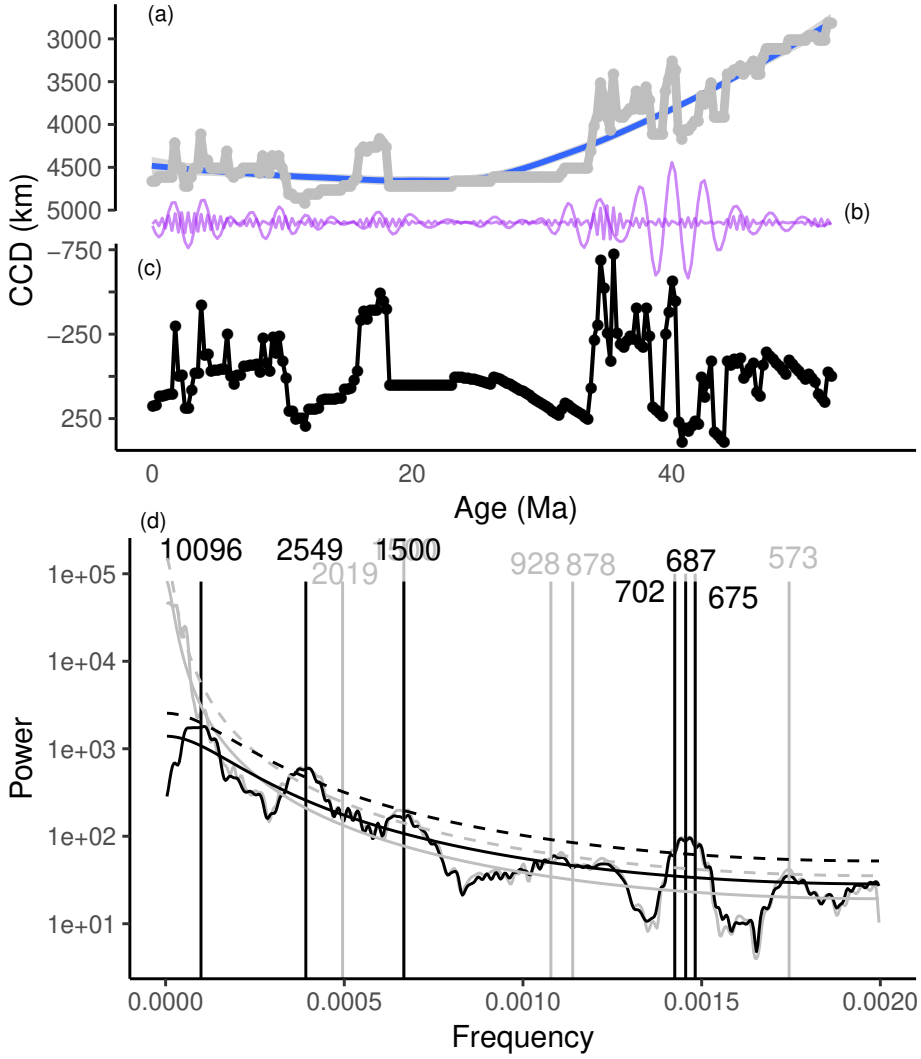

Figure 2. CCD as reconstructed by Pälike et al. (2012) (a), filtered for 405 kyr and 2.4 Myr (b) with a loess fit (a, blue line) subtracted from the record (c), which result in power spectra for the original (gray) and detrended (black) Pacific CCD composite (c). Significant peaks are labelled with the corresponding periods.

Table 1. Periods of interest in the input forcing were calculated from dominant secular frequencies (g, from Laskar et al. (2004)). Non-eccentricity typical periods were found visually with by analysing in detail the MTM-spectra of component. The index i in g_i refers to the planet in the solar system (counting from the sun outward).

Component	Terms	Period (yr)	Plot period (kyr)
Eccentricity	$g_4 - g_3$	2365408.22085889	2365
Eccentricity	$g_1 - g_5$	972584.643914338	973
Eccentricity	$g_2 - g_1$	696021.261160021	696
Eccentricity	$g_2 - g_5$	405691.71449262	405
Eccentricity	$g_2 - g_4$	123854.477912872	124
Eccentricity	$g_4 - g_5$	94886.4059134611	95
Obliquity			52.4
Obliquity			40.2
Obliquity			29.5
Obliquity			28.5
Precession			23.42
Precession			22.15
Precession			18.78
Precession			16.34

3 Effects of shifting records for consistency in overlap

Attempts were made to improve inter-record compatibility by shifting record $\delta^{13}C$ and $\delta^{18}O$ values from the various studies towards heavier or lighter values, such that mean isotope values in overlapping regions would be identical, but were eventually abandoned because of their minor influence on spectral outcome (Supp. Fig. 3).

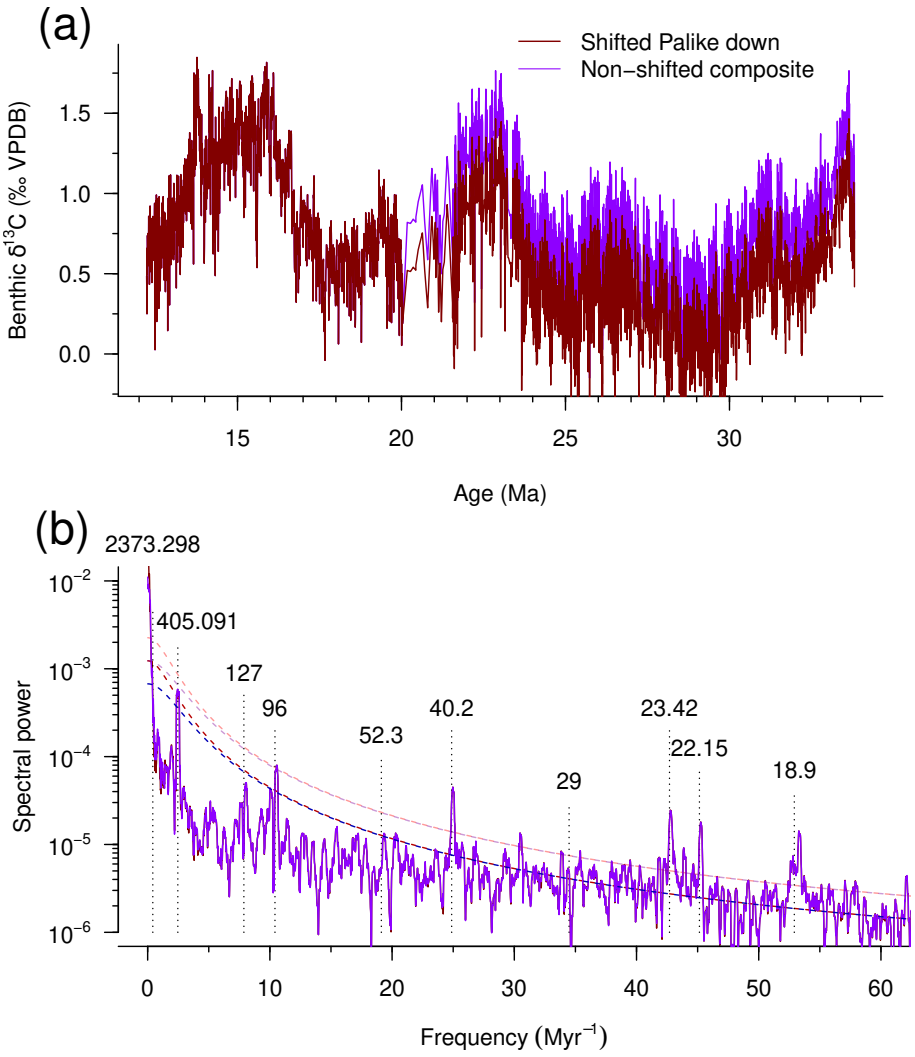

Figure 3. A linear shift in the record by Pälike et al. (2006) (down by $0.30\,‰$ VPDB in red, original in blue) increases consistency between records in the area of overlap (where data from Pälike et al. (2006) were omitted due to lower resolution) but hardly effects spectral outcome and is therefore not used in this study.

Table 2. Effects of increasing various parameters on model output.

Increased parameter	Causes this effect
initial pCO_2	Base level of $\delta^{13}C$ increases
`orbstrength`	Amplitude of cycle variation in tracers increases
`cliplevel`	Increased shift in spectral power to lower frequencies
`E`, `T` and `P` in `ETP`	Shift spectral power to associated frequencies
`noiselevel`	Amplitude of noise increases, base of AR-1 fit in MTM-spectra is raised
`noisetiming`	More noise is generated in lower frequency range

4 Model sensitivity

The introduction of white noise on C_{org} burial results in red noise in the spectral output of the model tracers. This basically means that the low-frequency spectral power amplification that we see in the orbitally-forced runs also occurs for the noise input. The addition of noise thus adds spectral power to the low-frequency range, and raises the background levels of MTM-spectra in the orbitally-forced model output tracers.

The model responds as expected to changes in initial conditions and newly added parameters. Table 2 shows an overview of what happens to the model output when a parameter is increased.

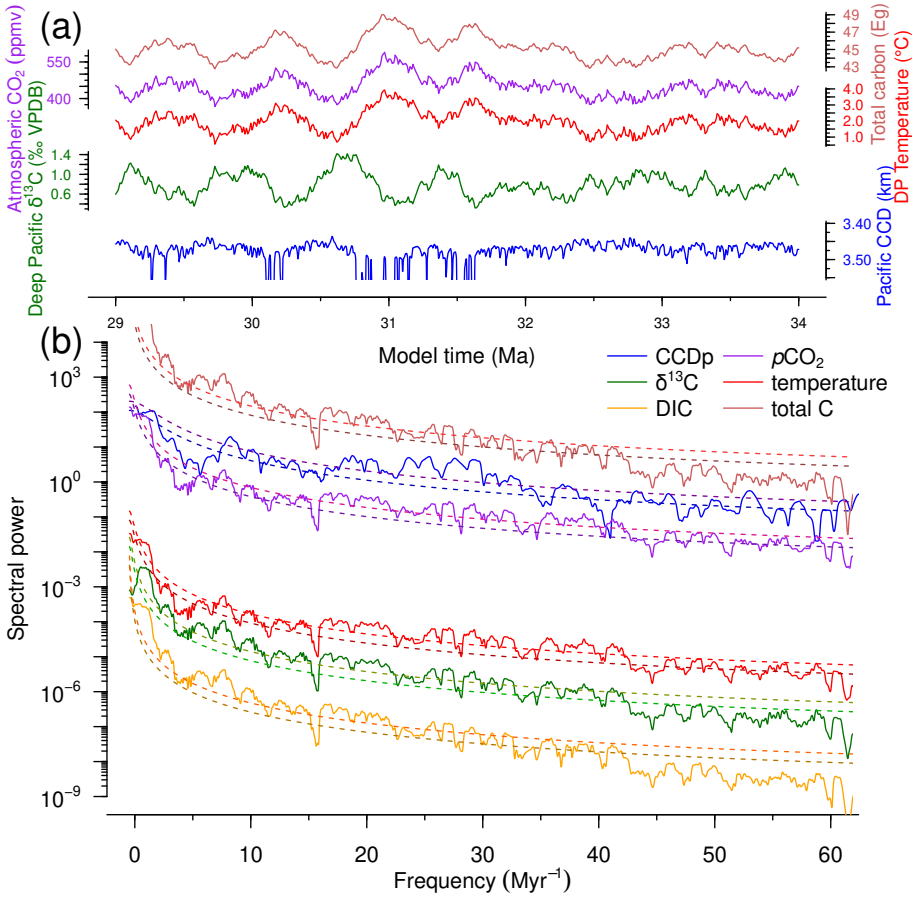

Figure 4. Model output when C_{org} burial is only affected by noise that is generated every time a time step larger than 1 kyr has passed in the time (A) and frequency (B) domain.

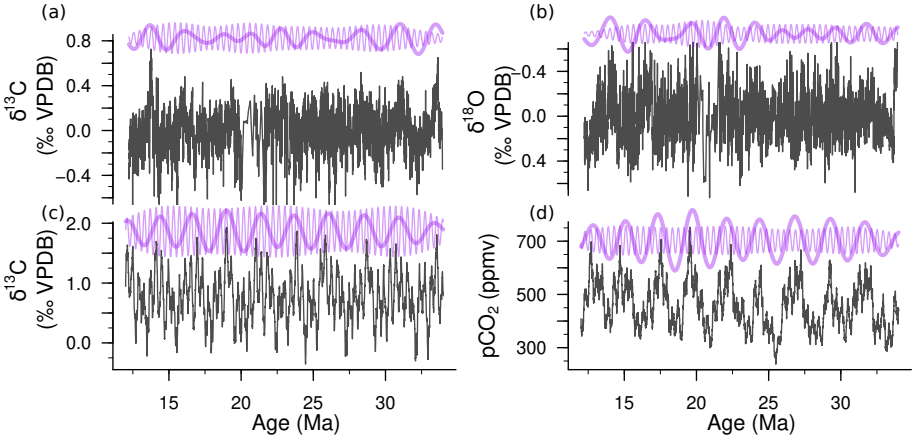

Figure 5. Comparison of the detrended data composite of δ^{13}C (a) and δ^{18}O (b) to model output δ^{13}C (c) and $p\mathrm{CO}_2$ (d) forced with ETP (1:0.5:−0.4) with an `orbstrength` of 0.5 and `noiselevel` of 0.2. 2.4 Myr and 405 kyr bandpass filters are shown in purple (shifted up by arbitrary amount).

5 Apparent lead in 2.4 Myr of the $-\delta^{13}C_{DP}$ signal

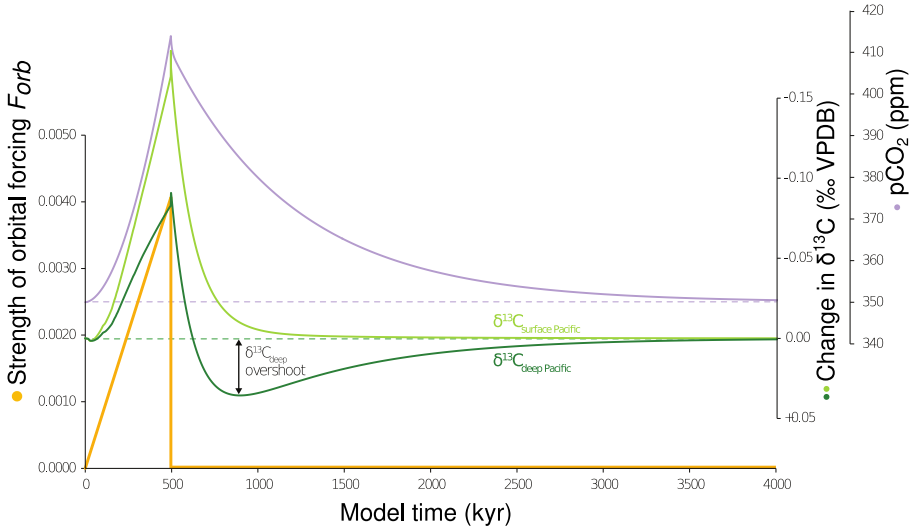

Figure 6. Transient linearly increasing orbital forcing (orange line) and the response of $\delta^{13}C$ (green line) and pCO_2 (purple line). Horizontal dotted lines are visual aids to track the initial values of $\delta^{13}C$ and pCO_2. The double arrow marked "$\delta^{13}C$ overshoot" is drawn between the initial value of $\delta^{13}C$ and the maximum value reached after cessation of forcing.

The δ^{13}C of DIC in deep and intermediate ocean boxes shows a lead to the $2.4\,$Myr eccentricity forcing. A close assessment of the first few peaks in the $2.4\,$Myr bandpass filtered deep-ocean δ^{13}C reveals that the lead only appears from the second peak onward, indicating that it may be an overshoot in the carbon isotope response to the forcing. Simulations with a transient, linearly increasing forcing were performed to explore whether the proposed overshoot could be found (Fig. 6). In this simulation, the imposed forcing decreased net burial of C_{org} for $500\,$kyr. During this time, pCO_2 progressively increases while δ^{13}C of DIC becomes more depleted. After the forcing has been terminated at $t = 500\,$kyr, pCO_2 slowly decreases to its initial value over millions of years by the feedback of continental weathering. In contrast, carbon isotopes return to their initial value much more rapidly and subsequently overshoot past it. A maximum δ^{13}C value is reached at $t = 895\,$kyr, almost $400\,$kyr after the forcing has stopped. This confirms that the observed lead of carbon isotopes to the $2.4\,$Myr eccentricity cycle is an overshoot response rather than an actual lead. Additionally, the slow development of the overshoot explains why it does not result in a lead to the shorter 405 and $100\,$kyr cycles. The remaining question is why the overshoot develops in deep and intermediate ocean δ^{13}C, but not in the surface ocean (Fig. 4 and Fig. 6). At any time, the mean δ^{13}C value of an ocean box represents a balance between the magnitude of carbon fluxes going in and out of the box and their isotopic signature. The LOSCAR model shows similar results as the box model runs by Kump (1991), which reveal that at steady state, surface ocean δ^{13}C follows the following equation:

$$\delta^{13}\mathrm{C}_{\mathrm{surface}} = \delta^{13}\mathrm{C}_{\mathrm{weathering}} - \Delta^{photo} \times (F^{OC}_{burial}/[F^{OC}_{burial} + F^{IC}_{burial}]) \quad (1)$$

Surface ocean δ^{13}C thus depends on three factors: the ratio between burial rates of organic (F^{OC}_{burial}) and inorganic carbon (F^{IC}_{burial}), the δ^{13}C of weathered carbon ($\delta^{13}C_{\mathrm{weathering}}$), and the magnitude of isotopic fractionation during photosynthesis (Δ^{photo}). As δ^{13}C weathering and Δ^{photo} are constant parameters in the model, δ^{13}C surface becomes lighter when relatively less organic carbon is buried, and vice versa. The carbon isotopic gradient between surface and deep ocean δ^{13}C can then be calculated according to the following equation (Broecker and Peng, 1982; Tyrrell and Zeebe, 2004):

$$\Delta\delta^{13}\mathrm{C} = -\Delta^{\mathrm{photo}} \times \Delta[\mathrm{DIC}]/[\mathrm{DIC}]_{\mathrm{mean}} \quad (2)$$

While $\delta^{13}C_{\mathrm{surface}}$ is independent of internal oceanic processes, $\delta^{13}C_{\mathrm{deep}}$ is determined by Δ^{photo} and the ratio between deep and surface DIC (Δ[DIC]) compared to the mean DIC of the ocean ($[\mathrm{DIC}]_{mean}$). As Δ[DIC] is dominantly controlled by the organic carbon pump, this can be interpreted as maintenance of the surface-to-deep isotope gradient by the biological pump.

Since both Δ^{photo} and the strength of the biological pump are constant in the model, changes in the gradient are mainly caused by the size of the total oceanic carbon inventory, reflected by $[\mathrm{DIC}]_{\mathrm{mean}}$. During the first $500\,$kyr of the simulation, both δ^{13}C surface and δ^{13}C deep become more ^{13}C-depleted as C_{org} burial is decreasing relative to IC burial. After the forcing has terminated, C_{org} burial instantaneously increases back to initial conditions. However, $[\mathrm{DIC}]_{\mathrm{mean}}$ and pCO_2 are still enhanced relative to the initial conditions for several Myr, thereby elevating both silicate and carbonate weathering (equations 1 and 2). During this rebound phase, δ^{13}C surface slowly increases back to its initial value, as burial of IC is enhanced relative to C_{org} burial. In addition to this, the elevated inventory of oceanic carbon diminishes the isotope gradient by decreasing $\Delta[\mathrm{DIC}]/[\mathrm{DIC}]_{\mathrm{mean}}$ (the small increase in Δ[DIC] is negligible compared to that in $[\mathrm{DIC}]_{\mathrm{mean}}$). This can be interpreted as a relative decrease in strength of the organic carbon pump compared to the size of the total carbon inventory, causing the deep isotopes to increase even more than those of the surface and resulting in the observed overshoot of $\delta^{13}C_{\mathrm{DP}}$.

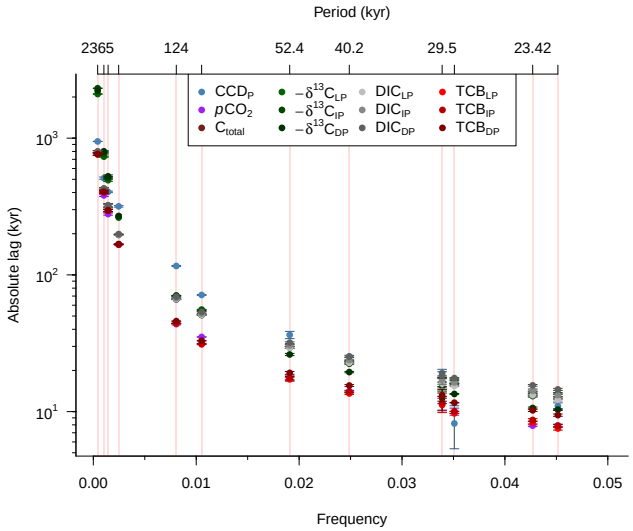

Figure 7. Absolute phasing (lags and leads indistinguishable) in absolute ages (kyr, log axis) as a function of frequency (cycles/kyr).

6 2.4 Myr amplitude modulation of the shorter eccentricity cycles

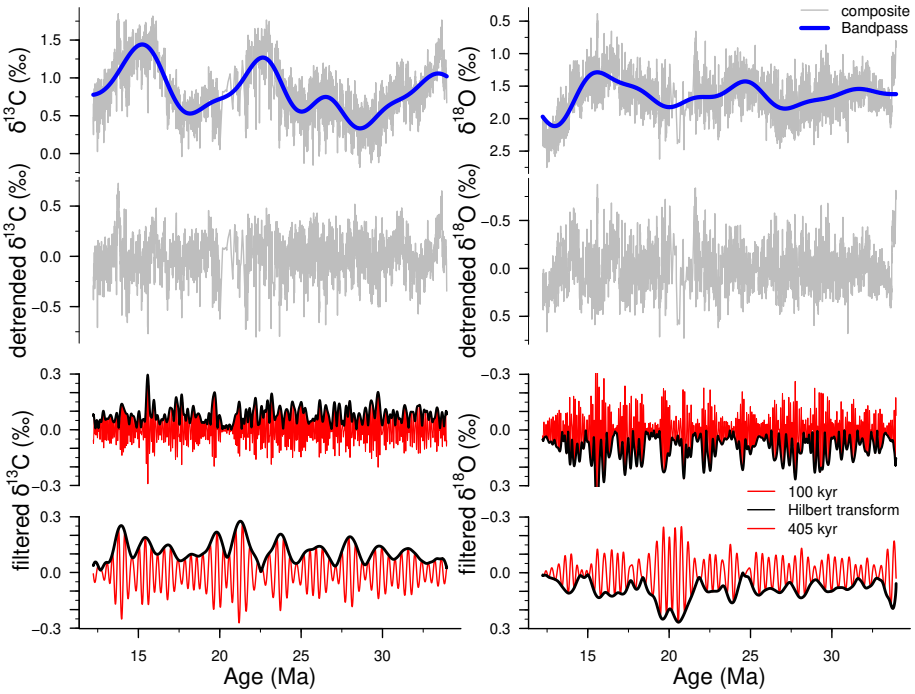

Figure 8. The envelopes (black) of the 100 and 405 kyr filtered (red) composite record (gray) show a clear 2.4 Myr cycle in δ^{13}C (left side) and δ^{18}O (right side). This is additional evidence for 2.4 Myr amplitude modulation of the 100 and 405 kyr eccentricity cycles.

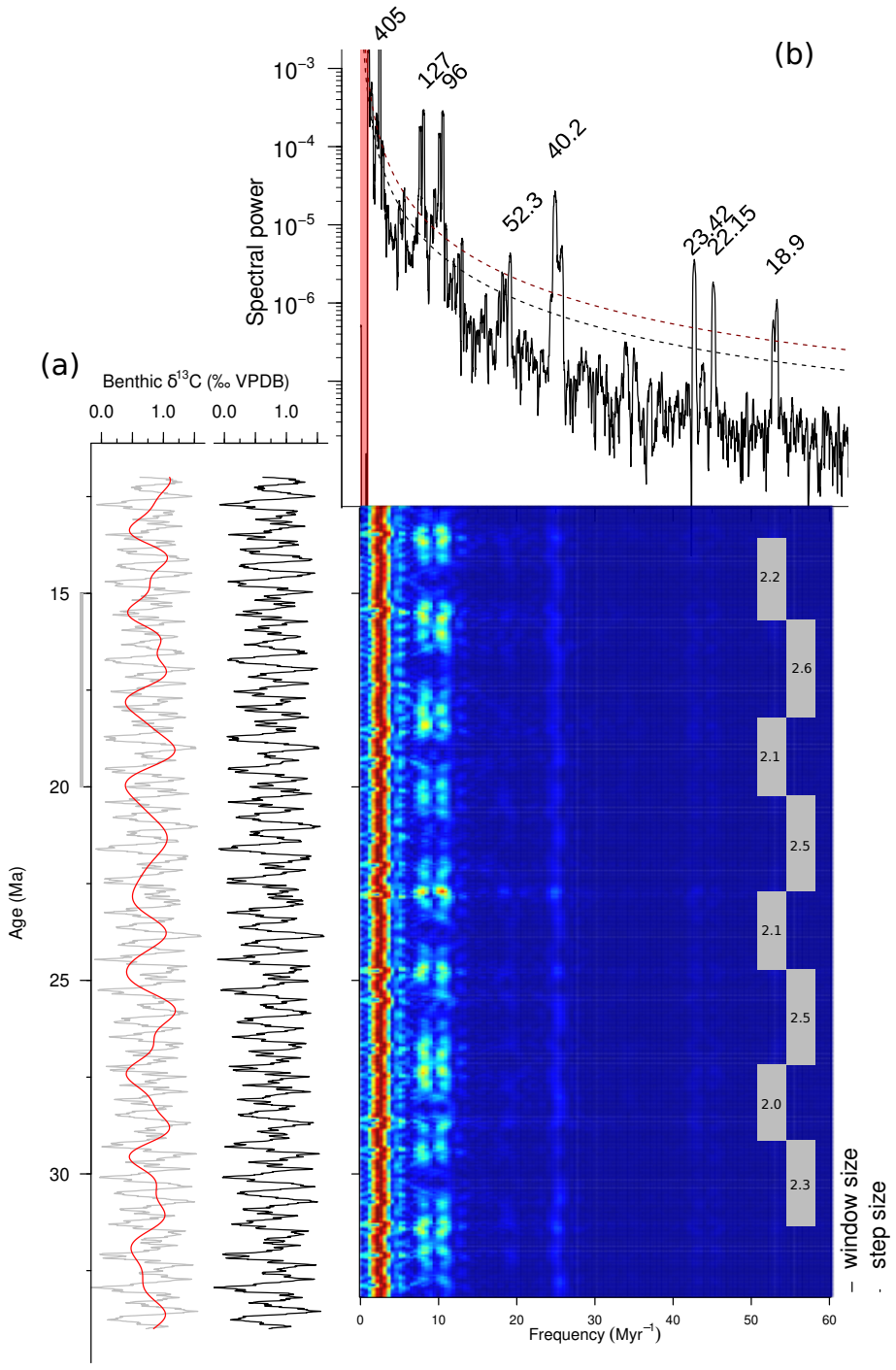

Figure 9. Evolutive multitaper harmonics analysis (c) of the model output δ^{13}C (grey) after detrending (black) the <1 Myr signal (red line) in the time (a), frequency (b) domain. Periods of interest are labelled (b) at the same axis as (c). Distances between peaks in the 100 kyr period of short eccentricity are marked (gray boxes with duration). A window size of 0.7 Myr was used, with a step size of 10 kyr (lines on the right side in (c)). Methods adapted from Pälike et al. (2006).

References

Broecker, W. and Peng, T.-H.: Tracers in the sea, Lamont-Doherty Geological Observatory, Columbia University, 1982.

Kump, L. R.: Interpreting carbon isotope excursions: Strangelove oceans, Geology, 19, 299–302, https://doi.org/10.1130/0091-7613(1991)019<0299, 1991.

Laskar, J., Robutel, P., Joutel, F., Gastineau, M., Correia, a. C. M., and Levrard, B.: Astrophysics A long-term numerical solution for the insolation, Astronomy, 285, 261–285, https://doi.org/10.1051/0004-6361, http://www.edpsciences.org/10.1051/0004-6361:20041335, 2004.

Pälike, H., Norris, R. D., Herrle, J. O., Wilson, P. A., Coxall, H. K., Lear, C. H., Shackleton, N. J., Tripati, A. K., and Wade, B. S.: The heartbeat of the Oligocene climate system., Science, 314, 1894–8, https://doi.org/10.1126/science.1133822, http://www.sciencemag.org/content/314/5807/1894.abstract{%}5Cnhttp://www.sciencemag.org/content/314/5807/1894, 2006.

Pälike, H., Lyle, M. W., Nishi, H., Raffi, I., Ridgwell, A., Gamage, K., Klaus, A., Acton, G., Anderson, L., Backman, J., Baldauf, J., Beltran, C., Bohaty, S. M., Bown, P., Busch, W., Channell, J. E., Chun, C. O., Delaney, M., Dewangan, P., Dunkley Jones, T., Edgar, K. M., Evans, H., Fitch, P., Foster, G. L., Gussone, N., Hasegawa, H., Hathorne, E. C., Hayashi, H., Herrle, J. O., Holbourn, A., Hovan, S., Hyeong, K., Iijima, K., Ito, T., Kamikuri, S. I., Kimoto, K., Kuroda, J., Leon-Rodriguez, L., Malinverno, A., Moore, T. C., Murphy, B. H., Murphy, D. P., Nakamura, H., Ogane, K., Ohneiser, C., Richter, C., Robinson, R., Rohling, E. J., Romero, O., Sawada, K., Scher, H., Schneider, L., Sluijs, A., Takata, H., Tian, J., Tsujimoto, A., Wade, B. S., Westerhold, T., Wilkens, R., Williams, T., Wilson, P. A., Yamamoto, Y., Yamamoto, S., Yamazaki, T., and Zeebe, R. E.: A Cenozoic record of the equatorial Pacific carbonate compensation depth, Nature, 488, 609–614, https://doi.org/10.1038/nature11360, http://dx.doi.org/10.1038/nature11360, 2012.

Tyrrell, T. and Zeebe, R. E.: History of carbonate ion concentration over the last 100 million years, Geochim. Cosmochim. Acta, 68, 3521–3530, https://doi.org/10.1016/j.gca.2004.02.018, 2004.

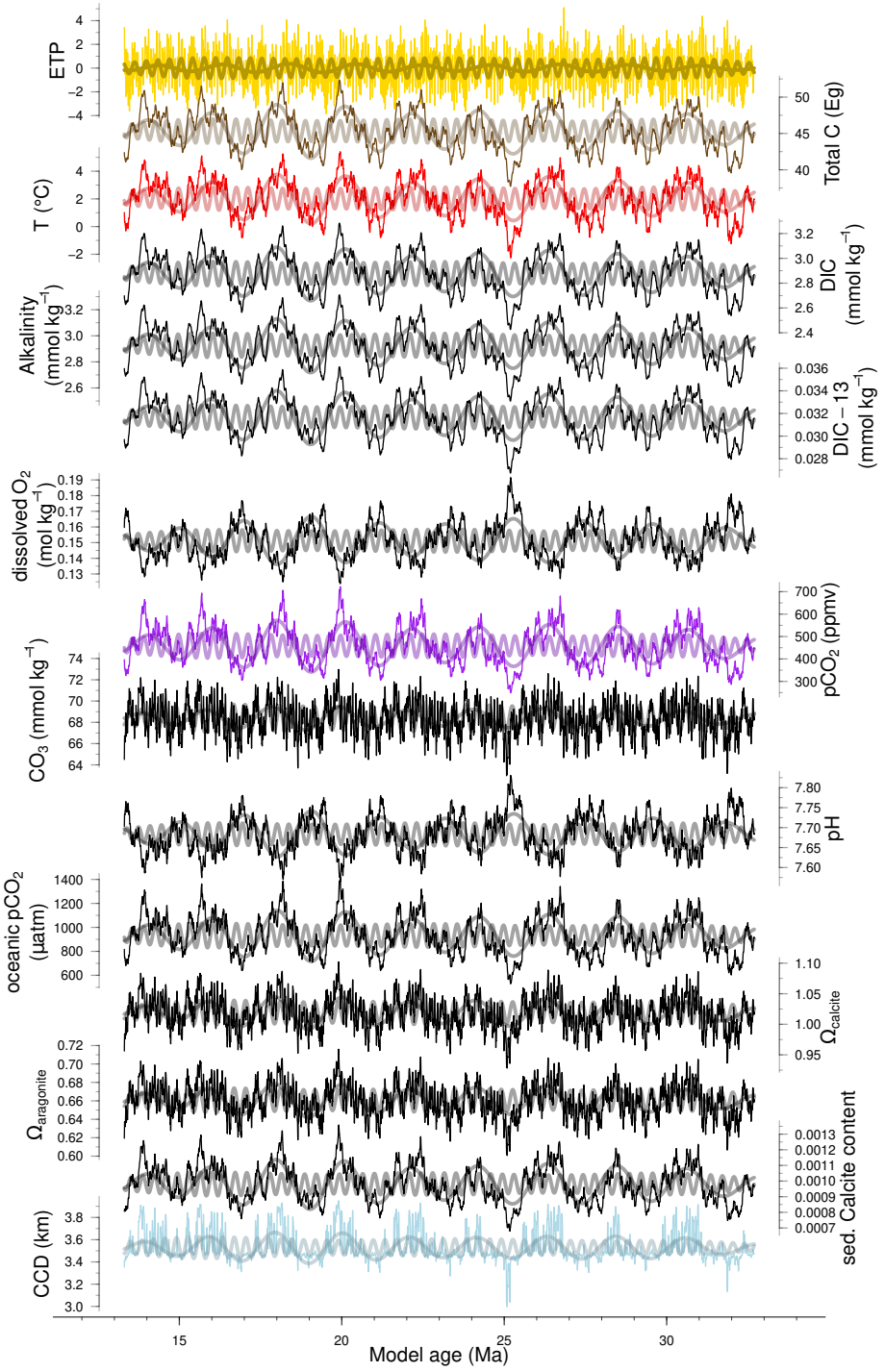

Figure 10. Example time-series model output for an ETP-forced (1:0.5:-0.4) run with `orbstrength` 0.5 and `noiselevel` 0, showing all model output tracers, except PO_4, because it is constant throughout at $2.62\,\mu\mathrm{mol\,kg^{-1}}$. 405 kyr (frequency of $2.46 \pm 0.15\,\mathrm{Myr^{-1}}$) and 2.4 Myr ($0.42 \pm 0.15\,\mathrm{Myr^{-1}}$) bandpass filters are shown for all records (thick darker lines).

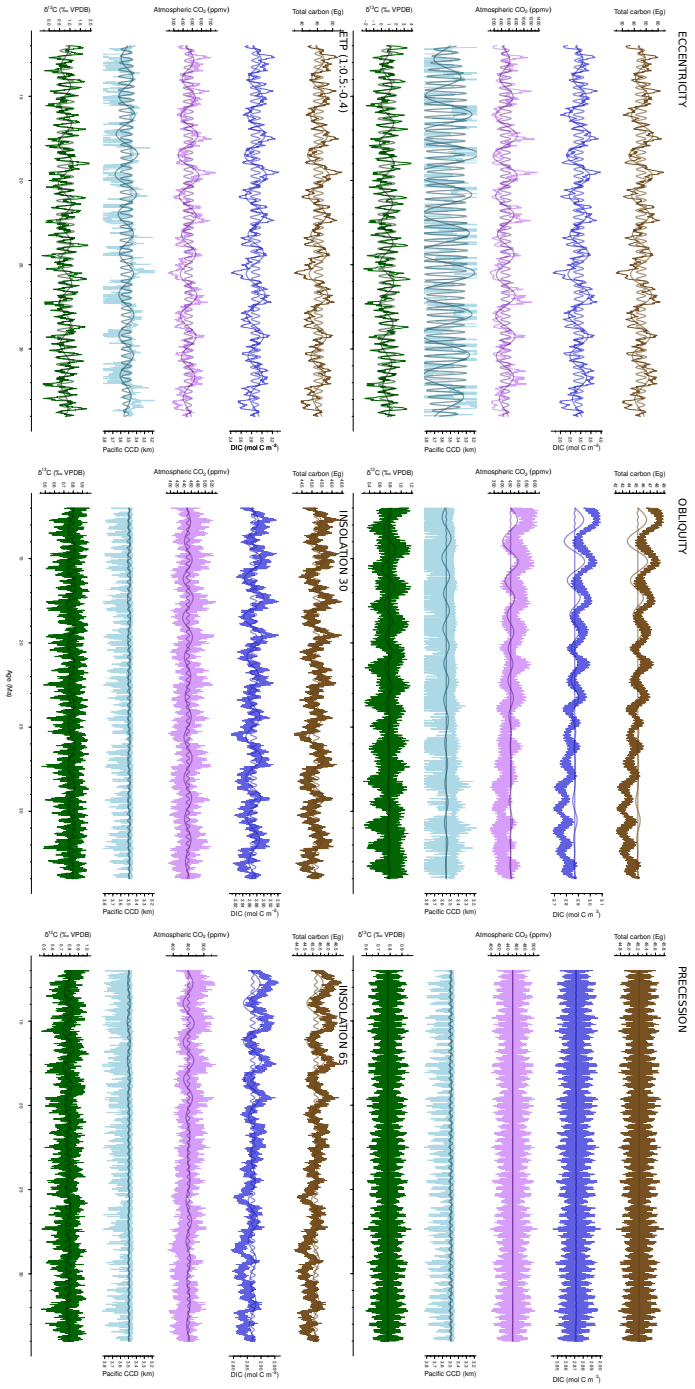

Figure 11. Time series model output with eccentricity, obliquity, precession, ETP (1:0.5:−0.4), 30°N and 65°N insolation forcing. Thick lines through the tracers represent 405 kyr and 2.4 Myr filters.